ACS OMEGA

Open Access

http://pubs.acs.org/journal/acsodf

Article

# Understanding the Selectivity of Selective Oxidation of Propane to Acrylic Acid on a Mo−Te−Nb−O M1 Catalyst Using Density Functional Theory

Karnajit Sen,* Ansgar Schäfer, Frank Rosowski, Dmitry I. Sharapa, and Felix Studt*

**Cite This:** *ACS Omega* 2026, 11, 11543−11554

**Read Online**

ACCESS | Metrics & More | Article Recommendations | Supporting Information

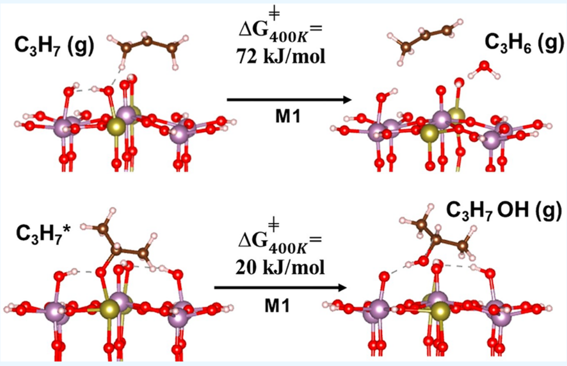

**ABSTRACT:** In this work, we have performed a quantum chemical investigation for the selective oxidation of propane toward acrylic acid on the M1 phase of a mixed metal oxide (MMO) catalyst, consisting of Mo−Te−Nb−O. The M1 phase of the catalyst has a complex surface structure, which involves different arrangements of metal sites with variable oxidation states. This complexity makes it inherently difficult to understand its activity and selectivity in catalytic reactions. We have used a multilayer cluster model of the main catalytically active site of M1 and a hybrid DFT methodology to establish the minimum energy pathways for the propane oxidation to acrylic acid via propylene, allyl alcohol, and acrolein as the key intermediates. In addition, the reactivity of propyl radicals toward the formation of isopropanol, which leads the reaction toward an unselective path of CO/$CO_2$ generation instead of acrylic acid production, has also been depicted. We show that the formation of isopropanol has rather a low activation barrier and is therefore competing with the formation of propylene from the propyl radical after C−H activation of propane. Once propylene has formed, the allyl position can easily be activated to form acrolein, which can be further oxidized to acrylic acid. In addition, we have developed a more general linear scaling relation for C−H activation chemistry to estimate activation barriers on M1 catalysts only based on four key energetic descriptors, which are the hydrogen binding energy ($E_H$) on the surface site, the C−H bond dissociation energy ($E_{BDE}$) of the reactant molecule in the gas phase, the interaction energy at transition state structure ($E^{TS}_{int}$), and the interaction energy between metal site and the oxygen atom of oxygenated gas molecules ($E_{MO}$).

## ■ INTRODUCTION

The activation of C−H bonds is an interesting topic as it often constitutes the first step for the functionalization of hydrocarbons toward higher-value chemicals. Usually, this activation is achieved through cofeeding oxygen, which often leads to oxygenated products that play an important role as a feedstock for many chemicals. However, these oxidation processes need to be highly selective, as one would otherwise obtain undesired side products, and here, in particular, $CO_2$. Devising heterogeneous catalysts that are highly selective is thus a crucial prerequisite for implementation in the chemical industry.[1,2] One example is given by the industrial conversion of propane to acrylic acid over the M1/M2 phase of a Mo−V−Te−Nb−O mixed metal oxide catalyst.[3−15] This catalyst has shown 61% selectivity for the conversion of propane to acrylic acid[16−19] at 380 °C. Relatively, selective oxidative dehydrogenation of both ethane and propane can also be achieved with this catalyst.[20−22]

This mixed metal oxide catalyst contains four metal elements and has a rather complex structure. It is believed that the (001) facet of bulk M1 is responsible for the observed catalytic activity.[23−25] This facet contains several structural motifs such as a five-membered ring of Mo surrounding Nb and six- and seven-membered rings of Mo/V surrounding Te.[26,27] There is also additional complexity from the variation of the element distribution and oxidation states of metal sites, such as $Mo^{6+}$/$Mo^{5+}$, $Mo^{6+}$/$V^{5+}$, $Mo^{5+}$/$V^{4+}$, $Te^{4+}$, $Te^{2+}$, and $Nb^{5+}$.

Deeper oxidation of propene produces various unwanted species, such as acetic acid, CO, or $CO_2$.[18] The formation of acetic acid occurs via degradation of acrylic acid[28] or via oxidation of acetone generated from propene via isopropanol in the presence of surface −OH species.[29,30] However, Naumann d'Alnoncourt et al.[18] observed that acetone is not a major byproduct of propane or propene oxidation. Acetone can only be detected at low conversion of propane; for conversions above 10%, the selectivity to acetone is often below 1%. For propylene as a feed, an increase in acetone

**Received:** September 15, 2025
**Revised:** January 9, 2026
**Accepted:** January 21, 2026
**Published:** February 8, 2026

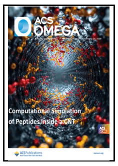

https://doi.org/10.1021/acsomega.5c09399

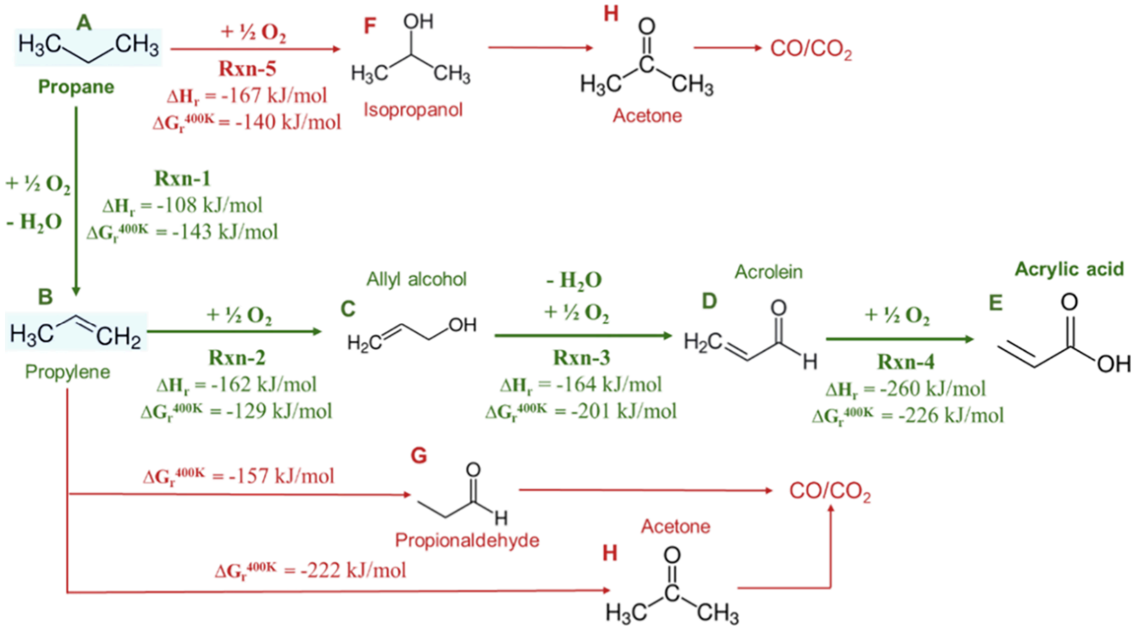

**Figure 1.** Schematic representation of the five reactions studied herein, inspired by Trunschke et al.[20] These include the four-step oxidation process of propane (A) to acrylic acid (E) via propene (B), allyl alcohol (C), and acrolein (D) as the intermediates (Rxn-1, -2, -3, and -4, green pathway). Rxn-5 represents the oxidation of propane to the unwanted byproducts isopropanol (F) and acetone (H). Pathways from propylene toward propionaldehyde (G) and acetone are also shown in red. Calculated reaction enthalpies ($\Delta H_r$) and Gibbs free energies at 400 K ($\Delta G_r^{400\ \mathrm{K}}$) from our DFT calculations (M06 functional) are shown.

selectivity toward 10% has been observed with increasing steam feed from 10 to 40%. Kube et al.[20] reported that activation of propane to propylene on M1 starts at a low temperature (120 °C), which shows that M1 can easily activate propane to produce valuable chemicals. They found that a quasi-simultaneous H abstraction on neighboring M═O sites based on kinetic isotope effects should be a more favorable pathway compared to first C−H activation at the middle carbon of propane and a subsequent radical-like pathway toward propene. They also reported the production of several intermediate gas species and overoxidation to $CO/CO_2$ with increasing reaction temperature (100−400 °C). Their proposed reaction network over a catalytic surface shows that propylene can be oxidized at all three carbon atoms to produce different oxygenated products. A selective pathway toward acrylic acid necessitates the oxidation of the allyl carbon atom to form allyl alcohol and acrolein as the intermediates. Oxidizing the central $sp^2$ carbon atom will lead to the formation of acetone, and oxidation of the terminal $sp^2$ carbon leads to propionaldehyde formation, with both being easily overoxidized to $CO/CO_2$.

Nevertheless, the reaction network from propane to acrylic acid is extremely complex and thus still not entirely understood.[10] Therefore, the selective propane oxidation using different transition-metal-based heterogeneous and homogeneous catalysts has been the subject of several theoretical studies.[31−33] It has been proposed that C−H abstraction and successive C−O bond formation at the allylic position of different gas-phase intermediates are the key steps in the above-mentioned pathways, which determine not only activity but also selectivity.[34] Liu et al. used the so-called H-atom addition energy (HAE), steric effects, and the effects of spin multiplicity to understand different active sites on the surface of M1.[34,35] They performed a comparative study for the activation of propane mainly at the porous site of M1 and on the (001) surface of $V_2O_5$ catalysts. Trunschke et al.[17,19] studied surface dynamics of the M1 phase of Mo−V M1 and Mo−V−Te−Nb M1 oxides in the presence and absence of steam during reaction conditions of propane oxidation to acrylic acid. Their studies claim that Te in the Mo−V−Te−Nb M1 oxide is a crucial element to gain selectivity, whereas Te-free Mo−V M1 oxide is also reported to be selective for acrylic acid production. Due to the large unit cell and complexity in terms of vanadium substitution and related oxidation states, simple models of M1 have been invoked. Goddard et al.[36,37] investigated the reduction-coupled oxo activation (ROA) mechanism for the conversion of propane to propene over a Te−V−Te cluster, where the propyl radical binds to the central V═O site after the first C−H activation, then transfers the second proton to a Te═O site, and finally dissociates from the surface to form propene. However, these models ignore the role of neighboring metal-oxo sites activating the C−H bond and their effect on the overall reaction mechanism. A study of ODH on M1 by Li et al.[38] shows a correlation between the adsorption energy of hydrogen atoms on the surface and the reaction energy and also the activation barrier of the C−H activation of alkanes, and they proposed a vertical migration of electrons from top to subsurface layers during the process.

In our previous study,[39] we established the full catalytic cycle for the oxidation of propane to propylene, exploring all possible phase spaces on the surface of our cluster model representing the active site of the M1 catalyst. We further showed that a universal linear scaling relation (LSR)[40−42] holds true for C−H activation of propane and propyl on M1. Using this LSR instead of explicitly calculating transition states and activation barriers dramatically speeds up the evaluation of microkinetics for the catalyst, considering all possible surface models of the catalytically active site. Our previous investigation also showed that, due to the electronic characteristics of M1, using density functional theory (DFT) on the

GGA level is not enough to produce accurate energies and that a hybrid DFT method is required.

In this work, our focus remains on the Mo-only model (shown in Figure 2) as a starting point, such that a simple scheme covering all reactions can be established, but note that highly active catalysts typically incorporate one or more V atoms.[27] The location and influence of vanadium on the catalytic activity are not fully understood to date. In this work, we have continued to investigate the reaction network starting from the propyl radical, followed by propylene toward acrylic acid. We have extended the LSR with three new parameters: (1) the C−H bond dissociation energy ($E_{\mathrm{BDE}}$) of the reactant molecule in the gas phase, (2) the interaction energy of the transition state structure ($E_{\mathrm{int}}^{\mathrm{TS}}$), and (3) the interaction energy between the metal site and the oxygen atom of the gas molecules ($E_{\mathrm{MO}}$). This extends the applicability to all relevant gas-phase intermediates. We have also introduced two different pathways, one for double bond formation via two successive CH activations and the other for insertion of oxygen in the activated radical species. This enables the study of the four selective reactions, such as propane to propylene (Rxn-1), propylene to allyl alcohol (Rxn-2), allyl alcohol to acrolein (Rxn-3), acrolein to acrylic acid (Rxn-4), and an unselective reaction that is propane to isopropanol in this work (as shown in Figure 1). Finally, the minimum energy pathways (MEPs) for these five reactions were determined after exploring all possible surface states of the highly dynamic active sites.

## ■ METHODS

All DFT calculations for cluster models were performed using the quantum chemistry molecular code TURBOMOLE.[43] Geometry optimizations have been performed within the generalized gradient approximation (GGA) using the PBE functional[44,45] with split valence basis sets (def2-SVP).[46] Single-point energy calculations have been performed for the optimized structures using the meta hybrid-DFT functional M06[47−49] and triple-$\zeta$ valence basis sets with two sets of polarization functions (def2-TZVPP)[46] for all data presented in this work (see Table ST5 in the SI for all PBE-D3 and M06-D3 energies). This approach is justified by the small differences when compared to fully M06-D3 optimized geometries (see Figures S14−S16, and Table ST9 in the SI for details). An extensive benchmark from Goerigk et al.[50] showed that adding D3 dispersion correction in general improved the description of noncovalent interactions and reaction energies. Therefore, the Grimme D3 dispersion correction[51] was applied for all our calculations (hence PBE-D3 and M06-D3).[50,52] This methodology has been shown to yield accurate energies for our cluster model as discussed in previous work.[39] Open shell calculations have been performed within the unrestricted Kohn−Sham framework.[53] We have explored the singlet, triplet, and quintet spin states for clusters with even numbers of electrons, and doublet, quartet, and sextet spin states for structures with odd numbers of electrons, and selected the spin state with the lowest energy to obtain the final single-point electronic energy.[39] All calculations have been performed on a four-layer cluster model of M1, shown in Figure 2, as this has been shown to be converged with respect to the number of layers, cluster size, fixed-atom constraints, oxidation states, and spin configurations.[39] During geometry optimizations, the top three layers were allowed to relax, whereas the atoms of the bottom layer were kept fixed in their bulk positions.[54−58] Hydrogen atoms of O−H have also been kept fixed (see also Figure 2).

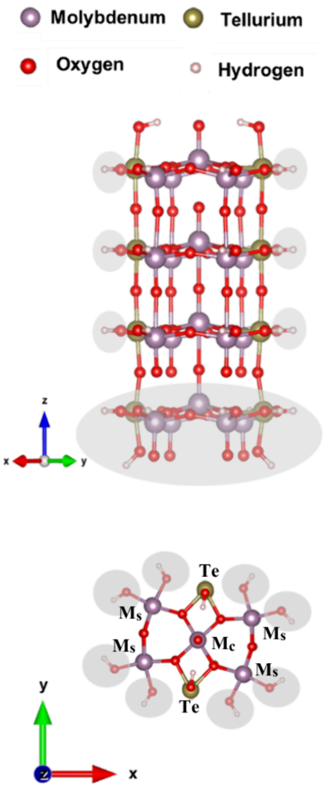

**Figure 2.** Side and top view of our four-layer cluster model of the catalytically active site of M1. Oxygen bridges to the surrounding bulk structure have been replaced by −OH groups (shown inside gray-colored circles). Each layer ($Mo_5Te_2$) of the cluster has one central $M_o$ (denoted by $M_c$), four symmetry-equivalent side-Mo (denoted by $M_s$), and two Te sites. The gray areas show the atoms that are kept fixed at their bulk positions during geometry optimizations. Reprinted in part with permission from J. Phys. Chem. C 2024, 128, 14273−14281. Copyright 2024 American Chemical Society.

Reaction barriers are calculated by scanning the reaction coordinates and performing constrained optimization at individual reaction coordinate values.[59] Zero-point energy (ZPE) corrections and entropy contributions are calculated from vibrational contributions (details are given in the SI). Reaction thermodynamics are obtained at 400 K and 1 bar. In order to calculate free energies of activation ($\Delta G_{\mathrm{TS}}$), we also need the entropic contribution TΔS. For this, we calculated an average value of 92 kJ/mol at 400 K for the entropies of the four transition states considered here (see Table ST2 and Figure S3 in the SI for details), a value which we will use throughout.

In order to investigate the thermodynamics of reactions in the gas phase, the structures of all gas-phase conformers of the molecular reaction intermediates have been optimized within the framework of DFT using the hybrid meta-GGA functional TPSSh[60] and basis sets of valence triple-$\zeta$ quality (TZVPP[61]). For the optimized structures, single-point energies have been calculated using the hybrid meta-GGA functional M06,[47−49] TZVPP basis sets, and Grimme's D3 dispersion correction. Zero-point vibrational energies, thermal corrections for enthalpies, and molecular entropies have been determined at 400 K and 1 bar in the rigid rotor/harmonic oscillator approximation using analytical second derivatives of the TPSSh energy with TURBOMOLE.

## ■ RESULTS AND DISCUSSION

### Thermodynamic Considerations

We start our analysis of the various reactions occurring during propane oxidation (see Figure 1) by considering the thermodynamics of the reactions in the gas phase (thus using molecular oxygen) and the comparison to surface reactions, where oxygen adsorbed on the catalyst surface is utilized. We do this for 3 different surface states of our catalysts with different degrees of oxidation. Each oxidation state has different possible surface configurations, and we always choose the most stable. These are labeled **6a**, **5a**, and **4a** in line with what we have published earlier and are shown in Figure 3, along with more reduced states **3a** and **2a**.[39] Note that during 2-electron oxidation (and thus 2-electron reduction of the catalyst), the oxidation states go from **6a** → **4a**, **5a** → **3a**, and **4a** → **2a**.

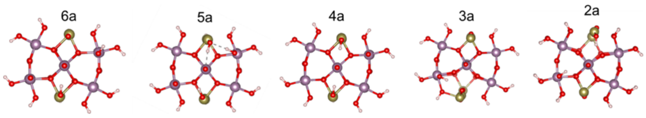

**Figure 3.** Five most stable surfaces configurations of the M1 catalyst active site for each surface oxidation state (SOX)−**6a**, **5a**, **4a**, **3a**, and **2a** (all surface configurations with their IDs are also presented in Table ST4 of the SI).

Table 1 shows the calculated Gibbs free energies of the propane oxidation pathways, shown in Figure 1, in the gas phase using molecular oxygen as the oxidant. This is compared to the three relevant M1 surfaces (initial states **6a**, **5a**, and **4a** and final states **4a**, **3a**, and **2a**; see Figure 3). Note that **3a** and **2a** cannot facilitate these reactions as they are in a reduced state and would need to be oxidized before the reaction.

The surface-configuration-dependent reactivity difference relative to the gas phase (last column in Table 1) depicts that all of the reactions become less favorable for more reduced catalyst surfaces. Furthermore, the difference in $\Delta G_r$ of the oxidation of propane to propylene (A → B) compared to the oxidation of propane to 2-propanol (A → F) is only about 3 kJ/mol. Since these two reactions have a similar thermodynamic driving force, the selectivity toward propylene instead of isopropanol is therefore determined by details of the reaction pathways with the associated kinetic barriers. Formation of isopropanol drives the reaction toward the unwanted formation of acetone (H) and overoxidation to $CO/CO_2$. After formation of propylene (B), the oxidations to acetone (B → H) or to propionaldehyde (B → G) are both thermodynamically more favorable than oxidation to allyl alcohol (B → C), which is the crucial intermediate to the formation of desired acrylic acid (E). However, the bond dissociation energy (BDE) of the allylic C−H bond of propylene is the lowest among all three carbon atoms in the molecule (all data provided in ST7 in the SI). Hence, the allylic C−H bond should be easiest to activate, which implies that selectivity toward acrylic acid will be driven by kinetics rather than by thermodynamics. In this study, we have not considered the formation of acetone and follow-up products, as we assume that once isopropanol is formed, this will eventually be overoxidized and lead to more oxidized products up to $CO_2$.

### Linear Scaling Relation

Having established the thermodynamics of the various reaction pathways over the catalytically relevant surfaces, we now turn our attention to the kinetics. Due to the large number of transition states that one would need to consider to achieve a comprehensive investigation, we will use estimations of barrier heights through the use of scaling relations.[40] We will make use of the scaling relations that we have established in our last work,[39] where we found a linear correlation of the C−H activation barrier of propane and of the propyl radical with the hydrogen binding energy ($E_H$) on the various catalytic surfaces of M1 in strong analogy to C−H activation over a range of materials (transition state structures and data are provided in Figure S2 and Table ST1 in the SI). For activation at the central C2 position in propane, the linear relation that we identified is

$$\Delta H_{TS} = 0.75 \times E_H + 175\ \text{kJ/mol} \tag{1}$$

Interestingly, the scaling relations for the activation of the different C−H bonds in propane, as well as in the propyl radical, all exhibited an identical slope but with different intercepts. Importantly, the differences in their intercepts could be related to the differences in C−H bond dissociation energies ($\Delta E_{BDE}$) according to

$$\Delta H_{TS} = 0.75 \times E_H + 175\ \text{kJ/mol} + \Delta E_{BDE} \tag{2}$$

where $\Delta E_{BDE}$ is the difference of the C−H bond dissociation energy in question, relative to that of the propane. In this work, we extend these considerations by including the C−H bond activation of propylene (B) and allyl alcohol (C), which are the relevant intermediates for acrolein and, ultimately, acrylic acid formation. In order to verify our approach, we calculated the transition states of C−H bond activation of propylene and allyl

**Table 1. Calculated $\Delta G_r^{400\ K}$ of the Oxidation Reactions in the Gas Phase Using Molecular Oxygen and on the Three Most Stable Surface Configurations 6a, 5a, and 4a (Ordering from More to Less Oxidized Surface) of the Cluster, Where the Surface Oxygen Atoms Are Utilized during Oxidation[a]**

| | calculated $\Delta G_r^{400\ K}$ in kJ/mol | | | | | | | |
|---|---|---|---|---|---|---|---|---|
| | A → B | A → F | B → H | B → G | B → C | C → D | D → E | reactivity differences |
| gas phase | −143 | −140 | −222 | −157 | −129 | −201 | −226 | |
| **6a** → **4a** | −139 | −136 | −218 | −153 | −125 | −196 | −222 | 4 |
| **5a** → **3a** | −90 | −87 | −169 | −104 | −76 | −148 | −173 | 53 |
| **4a** → **2a** | −55 | −52 | −134 | −69 | −41 | −113 | −138 | 88 |

[a] $\Delta G_r^{400\ K}$ shown for propane(A) → propylene(B), propane(A) → isopropanol(F), propylene(B) → acetone(H), propylene(B) → propionaldehyde(G), propylene(B) → allyl alcohol(C), allyl alcohol(C) → acrolein(D) and acrolein(D) → acrylic acid(E) (see also Figure 1 for reference of the various reactions). The last column depicts the differences between the reaction thermodynamics utilizing molecular oxygen and those over the three different catalyst states, where the surface oxygen atoms are utilized and reduced correspondingly.

alcohol over two catalytic surfaces (**6c** and **4g**), which represent two extreme values of $E_H$. The four new transition states are shown in Figure 4 and are taken relative to the reactants in the gas phase and the clean catalyst surface (please also see Figure S3, Table ST2 and raw data Tables ST6 and ST7 in the SI). Note that the transition states are depicted as $\Delta G$ at a temperature of 400 K, while we use $\Delta H_{TS}$ in our scaling relations, such that these are not convoluted by entropy differences. Figure 5a shows the dependence of the calculated activation enthalpies on hydrogen adsorption energies ($\Delta E_H$).

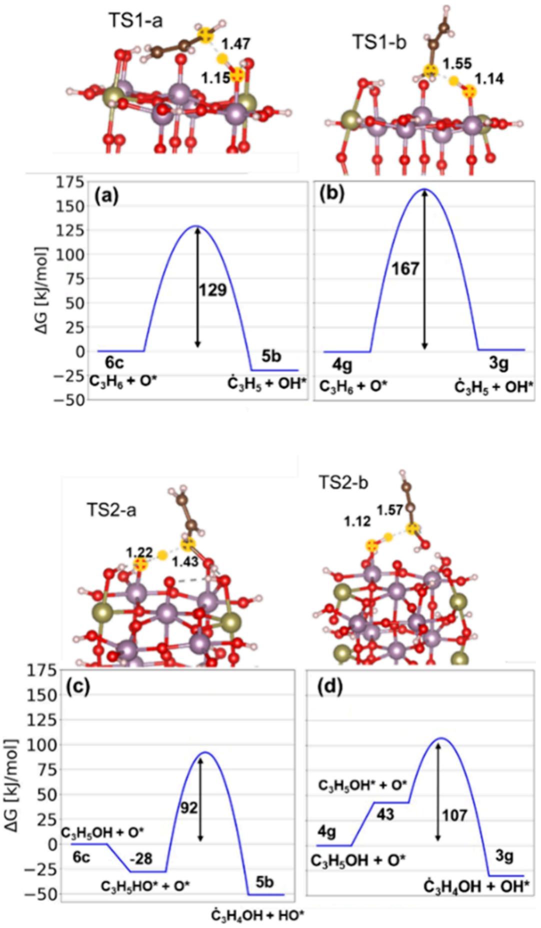

**Figure 4.** Transition states (with C−H−O bond distances in Å) and Gibbs free energy profiles for the of H abstraction on two different active site configurations (**6c** and **4g**), for propylene at the allylic carbon position (a) **6c** → **5b** (135 kJ/mol), (b) **4g** → **3g** (173 kJ/mol), and for allyl alcohol at C1 position (c) **6c** → **5b** (98 kJ/mol), (d) **4g** → **3g** (113 kJ/mol), at a temperature of 400 K.

The data are again well represented by a linear correlation with a slope of 0.75. However, in order to describe the intercepts accurately, two more factors needed to be included, such that the equation now reads:

$$\Delta H_{TS} = 0.75 \times E_H + 175\ \text{kJ/mol} + \Delta E_{BDE} + \Delta E_{int}^{TS} + E_{MO} \quad (3)$$

Here, we included the term $\Delta E_{int}^{TS}$, which is a correction for the transition state energy due to the interaction of the radical with the surface of the catalyst, as suggested from earlier work by Deshlahra et al. for the CH activation of different C1−C4 hydrocarbons and oxygenated molecules over Keggin-type polyoxometalate (POM) clusters.[32] They observed that Brønsted−Evans−Polanyi (BEP)-based LSRs, based only on the two main parameters $E_H$ and $D_{BDE}$, omit critical interactions between organic radicals and surface OH groups that form at transition states that mediate the H atom transfer, which depend on both molecular and catalyst properties. Further, deviations from linear relations caused by the lateness of transition states are also neglected. Deshlahra et al.[35] included these effects through crossing potential formalisms that account for the lateness in transition states, estimating activation energies, and estimating molecule-dependent but catalyst-independent parameters that account for diradical interactions using $\Delta E_{int}^{TS}$ that differ significantly when comparing allylic and nonallylic C−H bonds. The calculated data from their work, and also in this work, show that this diradical interaction term captures the destabilization of the allylic radical and can explain the lower yield of products from unsaturated hydrocarbon activation. This term explains the interaction of radical hydrocarbon species via its localized electron density at the activated carbon center, with the surface metal−OH site being part of the transition state. The differences of $\Delta H_{TS}$ to that of the secondary carbon of propane are well described by $\Delta E_{BDE}$ for saturated C3 molecules; however, there is a destabilization observed for the CH activation barrier of unsaturated hydrocarbons, the propylene molecule in our case (please refer to the Figure S4 in the SI). This destabilization is explained by the reduced interaction energy of $\Delta E_{int}^{TS}$ due to delocalization of electron density of the activated carbon via its unsaturated $\pi$ bond (explained in Figures S5−S8 in the SI). The second term that we introduced, $E_{MO}$, is an additional stabilizing energy originating from the interaction of an O-containing functional group in the reacting molecule with the catalyst surface metal site and via hydrogen bonding with a neighboring M−OH site if present. This can be seen in the transition state structures in Figure 4c,d, where we observed that allyl alcohol comes significantly close to a neighboring metal site via its oxygen. To elaborate this further, we have studied the adsorption of different O-containing species, such as water, methanol, isopropanol, allyl alcohol, and acrolein, on different cluster surfaces (Figures S9 and S10 in the SI).[62] All oxygenated molecules have a high tendency to be weakly adsorbed on the metal site via their O atoms. This has also been shown in earlier work by Xu et al.,[63] who observed that the final transition state energy for a surface-stabilized (SS) mechanism depends on the adsorption energy of the reactant and product as a descriptor for the BEP relation.

While estimations of these interactions vary to some degree, we identified energies for $\Delta E_{int}^{TS}$ and $E_{MO}$ to be 21 and −21 kJ/mol, respectively. These values would thus also exactly cancel out if both are present in the reacting molecule, as is the case for allyl alcohol, thus keeping the model rather simple. All of the values of these three variables for the relevant gas molecules required for this work are listed in Table 2.

Importantly, this simple model performs quite well and is able to describe the transition states calculated with DFT, as can be seen in Figure 5a. Eq 3 can be used to predict all transition states in question, the results of which are compared to the actual DFT calculations in the parity plot in Figure 5b. As can be seen, our predictions hold quite well with an overall MAE of 4.6 kJ/mol, which is the observed accuracy of DFT when comparing trends,[64,65] thus validating our approach.

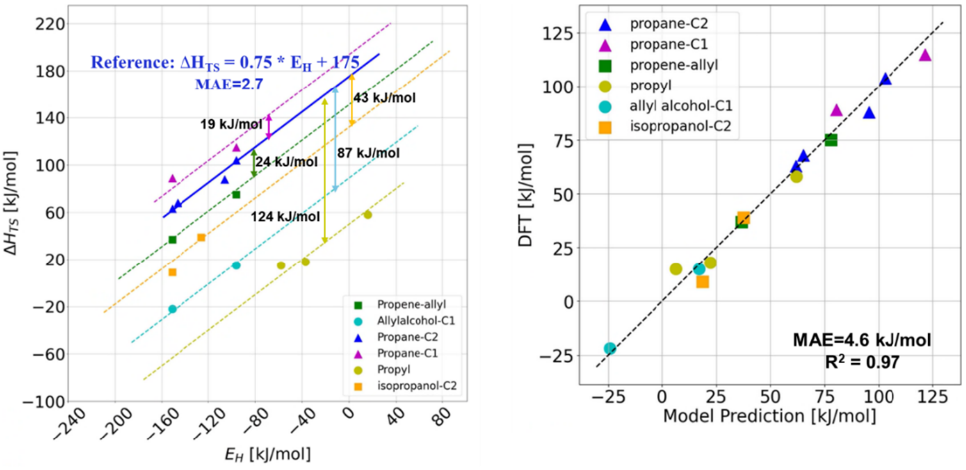

(a) (b)

**Figure 5.** (a) Linear scaling relations for C−H activation at C1 of propane (purple line), at C2 of propane (blue line), at C1 of 2-propyl (yellow line), at allylic carbon of propene (green line), and at C1 of allyl alcohol on the **Mo-only** M1 catalyst. Difference in interceptions are obtained from eq 3, and all slopes are kept at 0.75 × $E_H$. (b) Overall performance of our model in eq 3 as compared to DFT-calculated data, predicting most of the activation barriers with $R^2$ = 0.97 and MAE = 4.6 kJ/mol (the black line is the parity line). All of the data points are tabulated in Table ST8 in the SI.

**Table 2. Calculated $E_{BDE}$, $E_{int}^{TS}$, and $E_{MO}$ for 7 Different Relevant Gas Molecules Used in This Work ($E_{tot}$ = $E_{BDE}$ + $E_{TS}$ + $E_{MO}$)**

| gas molecule, position of H activation | $E_{BDE}$ (kJ/mol) | $\Delta E_{BDE}$ (kJ/mol) | $E_{int}^{TS}$ (kJ/mol) | $E_{MO}$ (kJ/mol) | $E_{tot}$ (kJ/mol) |
|---|---|---|---|---|---|
| propane C2 | 431 | 0 | 0 | 0 | **0** |
| propane C1 | 450 | +19[a] | 0 | 0 | **+19** |
| propylene, allylic position | 386 | −45 | 21 | 0 | **−24** |
| allyl alcohol, allylic position (C1) | 344 | −87 | 21 | −21 | **−87** |
| 2-propene-1-ol-1-yl, O−H | 191 | −240 | 21 | −21 | **−240** |
| acrolein C1 | 403 | −28 | 21 | −21 | **−28** |
| isopropanol C2 | 409 | −22 | 0 | −21 | **−43** |

[a] Ref 39.

## Minimum Energy Pathways

The thermodynamic calculations presented in Table ST3 of the Supporting Information (SI) reveal that the propyl radical adsorbs strongly onto the catalyst surface when a metal-oxo site of either molybdenum (Mo) or tellurium (Te) is present. Once adsorbed, fast migration of hydrogen atoms from neighboring metal−OH sites will lead to isopropanol formation. In our previous work,[39] we demonstrated that the free energy barrier for hydrogen migration between a metal−OH and a metal-oxo site is only about 20 kJ/mol (please refer to Figure S1 in the SI). Our calculations confirm that this low barrier also applies to hydrogen transfer from a neighboring metal−OH site to the oxygen atom, where the propyl radical is adsorbed (Figure 6b). This process leads to the immediate formation of 2-propanol, as illustrated in Figure S11 of the SI. The adsorption geometry of the propyl radical (shown in Figure S12 of the SI) suggests that the −OH group insertion is more favorable when the radical is adsorbed at a Te-oxo site compared to a Mo-oxo site. Based on these observations, we propose a second reaction pathway for the formation of oxygenated species. Note that this pathway depends crucially on the presence of a neighboring Mo/Te−OH site adjacent to the Mo/Te-oxo site, where the radical is adsorbed. On the other hand, in the absence of metal-oxo sites on the active site for radical adsorption, the activated radical molecule will abstract another hydrogen to a metal−OH site, forming an unsaturated C3 hydrocarbon and a water molecule. As we reported earlier, the CH abstraction from activated radical species (propyl in this case) is mostly barrierless.[39]

In the following section, we describe two reaction pathways that were used to determine the MEPs for the five reactions presented in Figure 1.

Figure 6a shows two consecutive H abstractions from the saturated C3 hydrocarbon at two different M-oxo and M-hydroxy sites, forming an unsaturated C3 molecule. Both activation barriers are estimated from the linear model in eq 3. This will describe Rxn-1 (propane to propylene) and Rxn-3 (allyl alcohol to acrolein). Figure 6b represents a 3-step process. First, the C−H abstraction occurs at a M-oxo site, followed by adsorption of the radical species on a M-oxo site, and finally, a H transfer from a neighboring M−OH site to the adsorbed fragment, forming isopropanol. The first C−H activation barrier is estimated from the linear model of eq 3, and the second barrier (H transfer) is assumed to be 20 kJ/mol, as estimated in the previous section. This pathway will describe Rxn-2 (propylene to allyl alcohol), Rxn-4 (acrolein to acrylic acid), and Rxn-5 (propane to isopropanol).

Our model of LSR in eq 3 is used to estimate the activation barriers for all H-abstraction steps. Since all these oxidation reactions are two-electron processes, the possible starting and ending SOX of the surfaces are 6 to 4, 5 to 3, and 4 to 2. We considered all possible pathways for all surface configurations. These are shown as dotted lines in Figure 7, whereas the bold green and red lines represent selective and unselective MEPs, respectively, at 400 K and 1 bar. Fast H-migration and the presence of −OH sites as a result of the presence of steam are included in our model as we connect all possible surfaces and pathways.

The free energy barriers for the first C−H activation of propane on the surfaces **6a**, **5a**, and **4a** are 142 kJ/mol, 215,

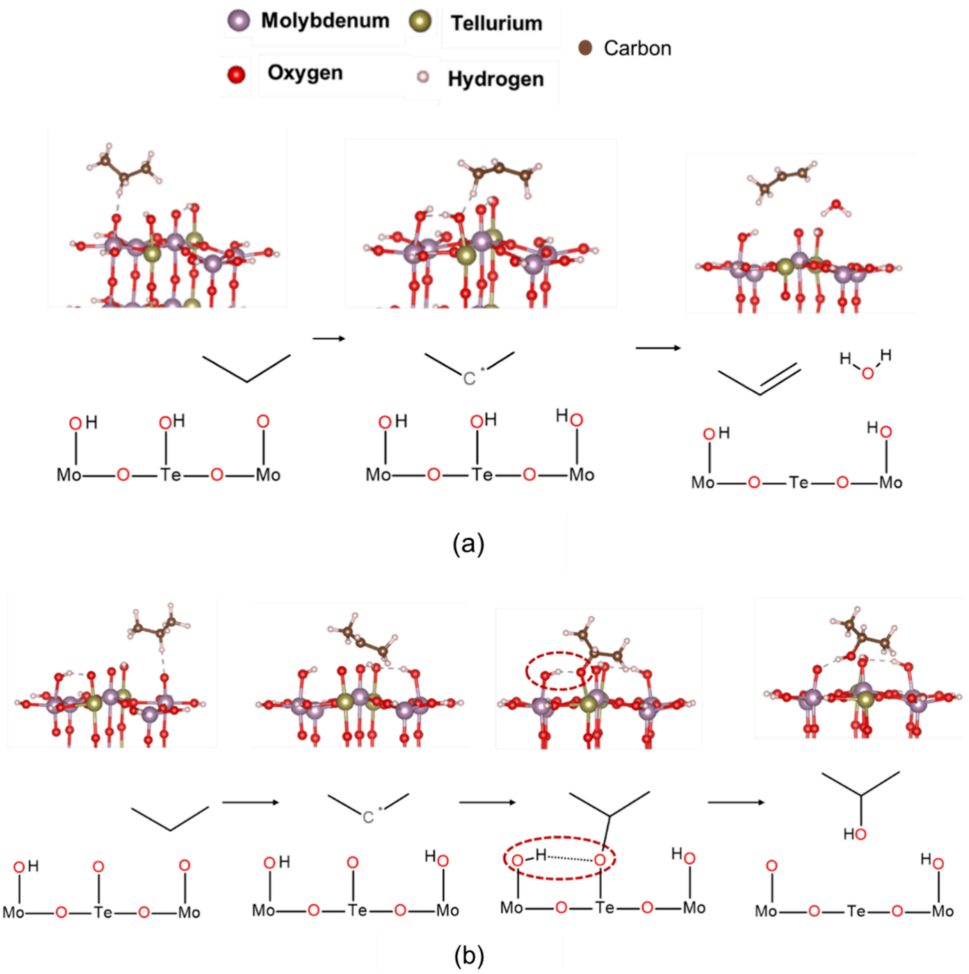

**Figure 6.** (a) Schematic description of the creation of a C═C double bond by two successive C−H bond activations of the two carbons of propane at two neighboring metal-oxo and metal−OH sites. The radical will not adsorb on the surface as there are no metal-oxo sites left; rather, it will abstract at another metal−OH site to create the alkene and a water molecule. In this case, the conversion of propane to propylene and water is shown as an example. (b) Schematic representation of the generation of a −OH group via a 3-step mechanism−first, C−H activation; second, radical adsorption on M═O; and finally, a fast H-migration from a neighboring M−OH to form and desorb the gas species. In this case, the conversion of propane to isopropanol is shown.

and 180 kJ/mol respectively, whereas the activation barrier to form propylene from propyl on the surfaces **5a**, **4a**, and **3g** are 115 kJ/mol, 76, and 163 kJ/mol, respectively (Figure 7a−c). The surface **6a** first isomerizes to **6d**, and propane is then activated on **6d**, rather than directly activating propane on **6a**.

The free energies of activation for allylic C−H bond abstraction in propylene in Rxn-2 on the surfaces **6a**, **5a**, and **4a** are 134 kJ/mol, 200 and 173 kJ/mol, respectively (Figure 7d−f). After the first C−H activation, the activated allyl radical will be adsorbed in a highly exothermic step on the surfaces **5a** (−113 kJ/mol) and **4a** (−117 kJ/mol). Subsequently, fast H-migration with a low barrier of 20 kJ/mol will create and desorb allyl alcohol from the surface, forming the surface states of **4a** and **3a**, respectively (Figure 7d, e). Although adsorption of the allyl radical can take place on surface **3a** (less exothermally with −60 kJ/mol), due to the absence of neighboring M−OH sites, the formation of allyl alcohol will not occur, as shown in Figure 7f. This situation causes the radical to remain adsorbed on the surface, blocking the active sites for other reactions to proceed from **3a**.

The free energies of activation for H abstraction from the C1 carbon in allyl alcohol in Rxn-3 on the surfaces **6a**, **5a**, and **4a** are 61 kJ/mol, 153, and 113 kJ/mol, respectively (Figure 7g−i). The activation barriers of 2-propylene-1-ol-1-yl radical on the surfaces **5a**, **4a**, and **3g** are 103 kJ/mol, 51, and 127 kJ/mol, respectively (Figure 7g−i). The pathways for formation of acrylic acid from acrolein in Rxn-4 are also presented in Figure 7j−l. The activation free energies at the C1 carbon in acrolein on the surfaces **6a**, **5a**, and **4a** are 133, 211, and 172 kJ/mol, respectively. Activated radical species will strongly adsorb on a M-oxo site of **5a** and **4a** with −290 and −270 kJ/mol, respectively. Again, a fast H-migration from a neighboring M−OH site with a 20 kJ/mol barrier creates the −OH group and facilitates the desorption of acrylic acid from the surface. Comparatively, a lower adsorption energy of −171 kJ/mol for the radical species of activated acrolein (2-propenal-1-yl) on **3a** is observed. However, this adsorbed species can block the surface sites since the lack of a neighboring M−OH site will not lead the reaction toward acrylic acid via the insertion of −OH.[66−84]

The formation of 2-propanol from propane in Rxn-5 is an unselective side path in the production of acrylic acid. The first C−H activation barriers are equal to the barriers for Rxn-1 (Figure 7m−o). The propyl radical will adsorb at the surfaces **5a** and **4a** with −121 and −82 kJ/mol, respectively. Consecutive H-migration will create isopropyl alcohol, which

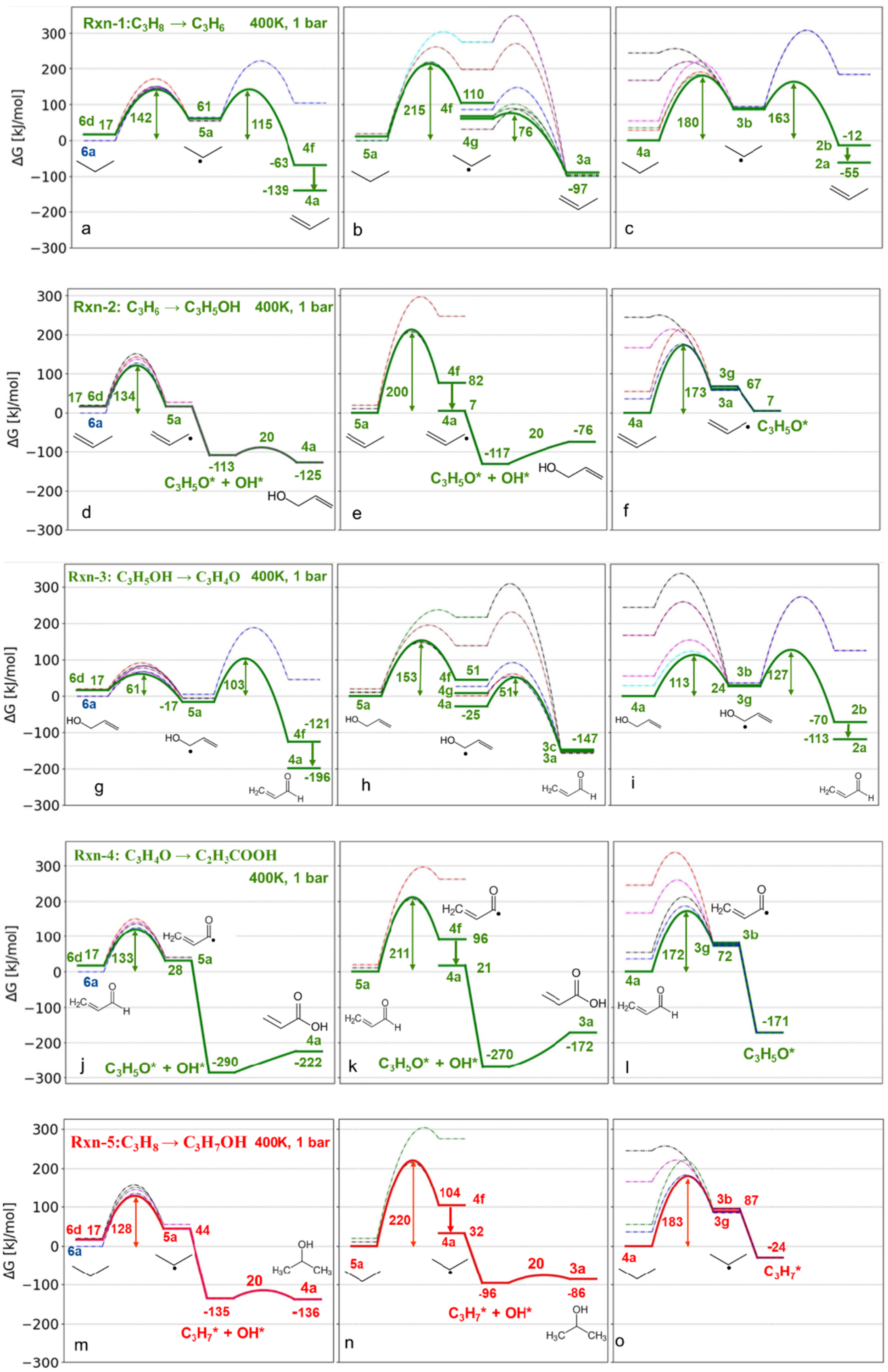

**Figure 7.** All calculated pathways (a−c: Rxn-1; d−f: Rxn-2; g−i: Rxn-3; j−l: Rxn-4; and m−o: Rxn-5) are shown for the surfaces **6a** → **4a**, **5a** → **3a**, **4a** → **2a** at 400 K, 1 bar. The green bold lines for the first four reactions in the selective path and the red bold lines for the unselective path of Rxn-5 represent the MEP, and dash-dotted lines represent other possible nonfavorable paths. All CH-activation barriers are estimated from the linear model of eq 3, and the H-migration barrier is kept constant at 20 kJ/mol.

consecutively desorbs from the surface at states **4a** and **3a**, respectively. This reaction is competing with the formation of propylene via C−H abstraction of propyl from the gas phase, which is barrierless (in energy) in most cases. Hence, we believe that the selectivity toward propylene should depend on the unavailability of a M═O adsorption site for propyl and the availability of M−OH sites for the further CH abstraction. This will lead to the conclusion that surface coverage of O* and OH* should be an important factor for selectivity of propylene. These two factors will drive the reaction toward unselective pathways to isopropanol, and the same two factors can increase the probability of −OH group insertion and the formation of allyl alcohol and acrylic acid in the oxidation of propylene and acrolein, respectively. All activation barriers of the MEPs are listed in Table 3.

Table 3. Free Energies of Activation $\Delta G_1^{TS}$ and $\Delta G_2^{TS}$ for the Five Reactions Studied on Three Different Starting Surfaces

| reactions (mechanism) | starting → end surfaces | $\Delta G_1^{TS}$ (kJ/mol) | $\Delta G_2^{TS}$ (kJ/mol) |
|---|---|---|---|
| Rxn-1: $C_3H_8 \rightarrow C_3H_6$ | 6a → 4a | 142 | 115 |
| | 5a → 3a | 215 | 76 |
| | 4a → 2a | 180 | 163 |
| Rxn-2: $C_3H_6 \rightarrow C_3H_5OH$ | 6a → 4a | 134 | 20 |
| | 5a → 3a | 200 | 20 |
| | 4a → 2a | 173 | |
| Rxn-3: $C_3H_5OH \rightarrow C_3H_4O$ | 6a → 4a | 61 | 103 |
| | 5a → 3a | 153 | 51 |
| | 4a → 2a | 113 | 127 |
| Rxn-4: $C_3H_4O \rightarrow C_2H_3COOH$ | 6a → 4a | 133 | 20 |
| | 5a → 3a | 211 | 20 |
| | 4a → 2a | 172 | |
| Rxn-5: $C_3H_8 \rightarrow C_3H_7OH$ | 6a → 4a | 142 | 20 |
| | 5a → 3a | 207 | 20 |
| | 4a → 2a | 166 | |

The surface **6a** isomerizes to **6d** and activates the C−H bond with a lower activation barrier in all five reactions shown above in Figure 7. For all cases shown, the C−H activation barrier on **5a** is always the highest among the three starting surfaces. The surface **5a** has three M−OH sites and only one M═O site. Hence, this indicates that high −OH coverage on the active site will lead to high C−H activation barriers. On the other hand, the MEPs show that Rxn-3 can occur on all the three starting surfaces, **6a**, **5a**, and **4a**, because of comparatively low barriers of allyl alcohol activation to produce acrolein. The same for Rxn-1 is favorable only on starting surfaces **6a** and **4a**. However, −OH insertion for Rxn-2, Rxn-4, and Rxn-5 is favorable only at **6a.** Because the CH-activation barrier at **5a** is very high, and −OH insertion starting from **4a** is hindered due to the lack of the M−OH site at **3a** for all the cases above. The mitigation for this problem is to keep the active site always at a high SOX of 6 by repeated oxidation by $O_2$.

The production of allyl alcohol from propylene and especially of acrylic acid from acrolein, both following the pathway depicted in Figure 6b, appeared to be less favorable and should become bottleneck reactions compared to the production of propylene from propane and acrolein from allyl alcohol, following the pathway depicted in Figure 6a, in the full pathway toward acrylic acid production. Naumann d'Alnoncourt et al.[18] reported that steam has no influence on the selectivity of propylene formation. However, Trunschke et al.[17] reported that the surface of M1 is enriched by $V^{5+}$ species in the presence of steam, which increases acrylic acid formation. In dry feed, surface $V^{5+}$ species are largely absent, and a reduced selectivity toward acrylic acid is observed. This observation can be correlated with the high computational activation barriers that we computed for acrylic acid pathways described above in the absence of vanadium at active sites.

Production of isopropanol is more favorable than production of propylene after propane activation. This should result in the reaction to drive toward the unselective pathway. Propylene is also easier to convert to acrylic acid due to lower activation barriers when compared to propane. Rapid hydrogen transfer at the metal site, which will possibly lead to the pathway shown in Figure 6b, is a key factor limiting the industrial viability of catalyst M1 for one-stage propane oxidation to acrylic acid, highlighting the need for a better understanding of these mechanisms to improve performance.

## CONCLUSIONS

In this work, we have extensively explored the phase space of catalytic surface configurations of the active site of the M1 phase of the Mo−Te−Nb−O catalyst and presented all plausible MEPs for the five most important reactions involved in the production of acrylic acid from the selective oxidation of propane. Furthermore, we have established a robust linear scaling model that can be applied to a broad range of gas-phase species reacting with oxide surfaces for a faster estimation of activation barriers. We believe that this framework is also potentially applicable to the activation of larger alkanes and radicals on Mo-type catalysts. Our results show that the high activation barrier for the first C−H activation on the Mo-only catalyst is the crucial rate-determining step of the entire process toward acrylic acid, a barrier that varies largely with the oxidation state of the surface. Furthermore, the availability of adjacent metal-oxo sites enables the adsorption of activated radical species, and a fast hydrogen migration from the neighborhood inserts the −OH group and desorbs the oxygenated molecule. Hence, a specific arrangement of surface M-Oxo and M−OH sites and surface coverage of O* and OH* species at reaction conditions are important descriptors for selectivity toward propylene and acrylic acid. This might be the ultimate bottleneck for the industrial implementation of a one-stage direct conversion of propane to acrylic acid via M1-type catalysts. However, how this picture will change with vanadium substitution as present in Mo−V−Te−Nb−O catalysts remains to be seen and requires further modeling, matching the complexity of the mechanistic aspects with those of catalyst modifications.

## ASSOCIATED CONTENT

### Supporting Information

The Supporting Information is available free of charge at https://pubs.acs.org/doi/10.1021/acsomega.5c09399.

DFT-calculated electronic energies for both at the PBE-D3 and M06-D3 level, ZPE and entropies at 298 and 400 K of all the ground state structures of the different surfaces of catalyst active sites and active sites with radical adsorbed, those are used in to develop MEP in Figure 7; electronic energies from PBE-D3 and M06-D3, ZPE and entropy at 400 K for all the transition state structures from Figures S2 and S3; DFT-calculated electronic energies for both at the PBE-D3 and M06-D3 level, ZPE and entropies at 298 and 400 K of all the gas molecules used in this work (PDF)

All the raw data from DFT (ZIP)

## AUTHOR INFORMATION

### Corresponding Authors

**Karnajit Sen** − *BASF SE, 67056 Ludwigshafen am Rhein, Germany;* orcid.org/0000-0002-4163-3969;
Email: karnajitsen@gmail.com
**Felix Studt** − *Institute of Catalysis Research and Technology (IKFT), Karlsruhe Institute of Technology (KIT), 76344*

*Eggenstein-Leopoldshafen, Germany;* orcid.org/0000-0001-6841-4232; Email: felix.studt@kit.edu

## Authors

**Ansgar Schäfer** − *Quantum Chemistry & Molecular Modeling, BASF SE, 67056 Ludwigshafen am Rhein, Germany*

**Frank Rosowski** − *BasCat, UniCat BASF JointLab, 10623 Berlin, Germany; BASF SE, Catalysis Research, 67065 Ludwigshafen, Germany*

**Dmitry I. Sharapa** − *Institute of Catalysis Research and Technology (IKFT), Karlsruhe Institute of Technology (KIT), 76344 Eggenstein-Leopoldshafen, Germany*

Complete contact information is available at: https://pubs.acs.org/10.1021/acsomega.5c09399

## Notes

The authors declare no competing financial interest.

## ■ ACKNOWLEDGMENTS

The authors specially thanks Dr. Annette Trunschke from FHI Berlin for valuable ideas and discussions and BASF SE to provide computational resources of their HPC machine for quantum chemical calculation.

## ■ REFERENCES

(1) Brazdil, J. F. Strategies for the Selective Catalytic Oxidation of Alkanes. *Top Catal* **2006**, *38* (4), 289−294.

(2) Li, X.; Teschner, D.; Streibel, V.; Lunkenbein, T.; Masliuk, L.; Fu, T.; Wang, Y.; Jones, T.; Seitz, F.; Girgsdies, F.; Rosowski, F.; Schlögl, R.; Trunschke, A. How to Control Selectivity in Alkane Oxidation? *Chem. Sci.* **2019**, *10* (8), 2429−2443.

(3) Védrine, J. Heterogeneous Partial (Amm)Oxidation and Oxidative Dehydrogenation Catalysis on Mixed Metal Oxides. *Catalysts* **2016**, *6* (2), 22.

(4) Faramawy, S.; Zaki, T.; Sakr, A. A.-E. Natural Gas Origin, Composition, and Processing: A Review. *Journal of Natural Gas Science and Engineering* **2016**, *34*, 34−54.

(5) Wachs, I. E.; Routray, K. Catalysis Science of Bulk Mixed Oxides. *ACS Catal.* **2012**, *2* (6), 1235−1246.

(6) Sprenger, P.; Kleist, W.; Grunwaldt, J.-D. Recent Advances in Selective Propylene Oxidation over Bismuth Molybdate Based Catalysts: Synthetic, Spectroscopic, and Theoretical Approaches. *ACS Catal.* **2017**, *7* (9), 5628−5642.

(7) Deshlahra, P.; Carr, R. T.; Chai, S.-H.; Iglesia, E. Mechanistic Details and Reactivity Descriptors in Oxidation and Acid Catalysis of Methanol. *ACS Catal.* **2015**, *5* (2), 666−682.

(8) Shiju, N. R.; Liang, X.; Weimer, A. W.; Liang, C.; Dai, S.; Guliants, V. V. The Role of Surface Basal Planes of Layered Mixed Metal Oxides in Selective Transformation of Lower Alkanes: Propane Ammoxidation over Surface *Ab* Planes of Mo−V−Te−Nb−O M1 Phase. *J. Am. Chem. Soc.* **2008**, *130* (18), 5850−5851.

(9) Andrushkevich, T. V.; Ovchinnikova, E. V. The Role of Water in Selective Heterogeneous Catalytic Oxidation of Hydrocarbons. *Molecular Catalysis* **2020**, *484*, No. 110734.

(10) Schlögl, R. Active Sites for Propane Oxidation: Some Generic Considerations. *Top Catal* **2011**, *54* (10−12), 627−638.

(11) Grasselli, R. K.; Buttrey, D. J.; Burrington, J. D.; Andersson, A.; Holmberg, J.; Ueda, W.; Kubo, J.; Lugmair, C. G.; Volpe, A. F. Active Centers, Catalytic Behavior, Symbiosis and Redox Properties of MoV(Nb,Ta)TeO Ammoxidation Catalysts. *Top Catal* **2006**, *38* (1−3), 7−16.

(12) Schlögl, R. Selective Oxidation: From a Still Immature Technology to the Roots of Catalysis Science. *Top Catal* **2016**, *59* (17−18), 1461−1476.

(13) Hävecker, M.; Wrabetz, S.; Kröhnert, J.; Csepei, L.-I.; Naumann d'Alnoncourt, R.; Kolen'ko, Y. V.; Girgsdies, F.; Schlögl, R.; Trunschke, A. Surface Chemistry of Phase-Pure M1MoVTeNb Oxide during Operation in Selective Oxidation of Propane to Acrylic Acid. *J. Catal.* **2012**, *285* (1), 48−60.

(14) Sanfiz, A. C.; Hansen, T. W.; Teschner, D.; Schnörch, P.; Girgsdies, F.; Trunschke, A.; Schlögl, R.; Looi, M. H.; Hamid, S. B. A. Dynamics of the MoVTeNb Oxide M1 Phase in Propane Oxidation. *J. Phys. Chem. C* **2010**, *114* (4), 1912−1921.

(15) Wernbacher, A. M.; Kube, P.; Hävecker, M.; Schlögl, R.; Trunschke, A. Electronic and Dielectric Properties of MoV-Oxide (M1 Phase) under Alkane Oxidation Conditions. *J. Phys. Chem. C* **2019**, *123* (21), 13269−13282.

(16) Duprez, D.; Cavani, F. *Handbook of Advanced Methods and Processes in Oxidation Catalysis: From Laboratory to Industry*; Imperial College Press, 2014.

(17) Trunschke, A.; Noack, J.; Trojanov, S.; Girgsdies, F.; Lunkenbein, T.; Pfeifer, V.; Hävecker, M.; Kube, P.; Sprung, C.; Rosowski, F.; Schlögl, R. The Impact of the Bulk Structure on Surface Dynamics of Complex Mo−V-Based Oxide Catalysts. *ACS Catal.* **2017**, *7* (4), 3061−3071.

(18) Naumann d'Alnoncourt, R.; Csepei, L.-I.; Hävecker, M.; Girgsdies, F.; Schuster, M. E.; Schlögl, R.; Trunschke, A. The Reaction Network in Propane Oxidation over Phase-Pure MoVTeNb M1 Oxide Catalysts. *J. Catal.* **2014**, *311*, 369−385.

(19) Amakawa, K.; Kolen'ko, Y. V.; Villa, A.; Schuster, M. E.; Csepei, L.-I.; Weinberg, G.; Wrabetz, S.; Naumann d'Alnoncourt, R.; Girgsdies, F.; Prati, L.; Schlögl, R.; Trunschke, A. Multifunctionality of Crystalline MoV(TeNb) M1 Oxide Catalysts in Selective Oxidation of Propane and Benzyl Alcohol. *ACS Catal.* **2013**, *3* (6), 1103−1113.

(20) Kube, P.; Frank, B.; Schlögl, R.; Trunschke, A. Isotope Studies in Oxidation of Propane over Vanadium Oxide. *ChemCatChem.* **2017**, *9* (18), 3446−3455.

(21) Donaubauer, P. J.; Melzer, D. M.; Wanninger, K.; Mestl, G.; Sanchez-Sanchez, M.; Lercher, J. A.; Hinrichsen, O. Intrinsic Kinetic Model for Oxidative Dehydrogenation of Ethane over MoVTeNb Mixed Metal Oxides: A Mechanistic Approach. *Chemical Engineering Journal* **2020**, *383*, No. 123195.

(22) Annamalai, L.; Liu, Y.; Ezenwa, S.; Dang, Y.; Suib, S. L.; Deshlahra, P. Influence of Tight Confinement on Selective Oxidative Dehydrogenation of Ethane on MoVTeNb Mixed Oxides. *ACS Catal.* **2018**, *8* (8), 7051−7067.

(23) Celayasanfiz, A.; Hansen, T.; Sakthivel, A.; Trunschke, A.; Schlogl, R.; Knoester, A.; Brongersma, H.; Looi, M.; Hamid, S. How Important Is the (001) Plane of M1 for Selective Oxidation of Propane to Acrylic Acid? *J. Catal.* **2008**, *258* (1), 35−43.

(24) DeSanto, P.; Buttrey, D. J.; Grasselli, R. K.; Lugmair, C. G.; Volpe, A. F.; Toby, B. H.; Vogt, T. Structural Aspects of the *M* 1 and *M* 2 Phases in MoVNbTeO Propane Ammoxidation Catalysts. *Zeitschrift für Kristallographie - Crystalline Materials* **2004**, *219* (3), 152−165.

(25) Li, X.; Buttrey, D. J.; Blom, D. A.; Vogt, T. Improvement of the Structural Model for the M1 Phase Mo−V−Nb−Te−O Propane (Amm)Oxidation Catalyst. *Top Catal* **2011**, *54* (10−12), 614−626.

(26) Masliuk, L.; Heggen, M.; Noack, J.; Girgsdies, F.; Trunschke, A.; Hermann, K. E.; Willinger, M. G.; Schlögl, R.; Lunkenbein, T. Structural Complexity in Heterogeneous Catalysis: Cataloging Local Nanostructures. *J. Phys. Chem. C* **2017**, *121* (43), 24093−24103.

(27) Grasselli, R. K.; Lugmair, C. G.; Volpe, A. F. Towards an Understanding of the Reaction Pathways in Propane Ammoxidation Based on the Distribution of Elements at the Active Centers of the M1 Phase of the MoV(Nb,Ta)TeO System. *Top Catal* **2011**, *54* (10−12), 595−604.

(28) Vitry, D.; et al. Mo-V-Te-(Nb)-O Mixed Metal Oxides Prepared by Hydrothermal Synthesis for Catalytic Selective Oxidations of Propane and Propene to Acrylic Acid. *Appl. Catal. A: Gen.* **2003**, *251* (2), 411−424.

(29) Trunschke, A.; Bellini, G.; Boniface, M.; Carey, S. J.; Dong, J.; Erdem, E.; Foppa, L.; Frandsen, W.; Geske, M.; Ghiringhelli, L. M.; Girgsdies, F.; Hanna, R.; Hashagen, M.; Hävecker, M.; Huff, G.;

Knop-Gericke, A.; Koch, G.; Kraus, P.; Kröhnert, J.; Kube, P.; Lohr, S.; Lunkenbein, T.; Masliuk, L.; Naumann d'Alnoncourt, R.; Omojola, T.; Pratsch, C.; Richter, S.; Rohner, C.; Rosowski, F.; Rüther, F.; Scheffler, M.; Schlögl, R.; Tarasov, A.; Teschner, D.; Timpe, O.; Trunschke, P.; Wang, Y.; Wrabetz, S. Towards Experimental Handbooks in Catalysis. *Top Catal* **2020**, *63* (19–20), 1683–1699.

(30) Botella, P.; López Nieto, J. M.; Solsona, B.; Mifsud, A.; Márquez, F. The Preparation, Characterization, and Catalytic Behavior of MoVTeNbO Catalysts Prepared by Hydrothermal Synthesis. *J. Catal.* **2002**, *209* (2), 445–455.

(31) Araujo-Lopez, E.; Vandeghuchte, B. D.; Curulla-Ferré, D.; Sharapa, D. I.; Studt, F. Trends in the Activation of Light Alkanes on Transition-Metal Surfaces. *J. Phys. Chem. C* **2020**, *124*, 27503–37510.

(32) Liu, Z.; Fan, S.; Tranca, I.; Tielens, F. Theoretical Investigation of Reaction Mechanisms of CoO+ with Propane. *Theor. Chem. Acc.* **2025**, *144* (6), 42.

(33) Liu, Z.; Guo, W.; Zhao, L.; Shan, H. Theoretical Investigation of the Oxidation of Propane by $FeO^+$. *J. Phys. Chem. A* **2010**, *114* (7), 2701–2709.

(34) Liu, Y.; Twombly, A.; Dang, Y.; Mirich, A.; Suib, S. L.; Deshlahra, P. Roles of Enhancement of C–H Activation and Diminution of C–O Formation Within M1-Phase Pores in Propane Selective Oxidation. *ChemCatChem.* **2021**, *13* (3), 882–899.

(35) Deshlahra, P.; Iglesia, E. Reactivity and Selectivity Descriptors for the Activation of C–H Bonds in Hydrocarbons and Oxygenates on Metal Oxides. *J. Phys. Chem. C* **2016**, *120* (30), 16741–16760.

(36) Cheng, M.-J.; Goddard, W. A. The Mechanism of Alkane Selective Oxidation by the M1 Phase of Mo–V–Nb–Te Mixed Metal Oxides: Suggestions for Improved Catalysts. *Top Catal* **2016**, *59* (17–18), 1506–1517.

(37) Cheng, M.-J.; Goddard, W. A. I. In Silico Design of Highly Selective Mo-V-Te-Nb-O Mixed Metal Oxide Catalysts for Ammoxidation and Oxidative Dehydrogenation of Propane and Ethane. *J. Am. Chem. Soc.* **2015**, *137* (41), 13224–13227.

(38) Li, W.-Q.; Fjermestad, T.; Genest, A.; Rösch, N. Reactivity Trends of the $MoVO_x$ Mixed Metal Oxide Catalyst from Density Functional Modeling. *Catal. Sci. Technol.* **2019**, *9* (7), 1559–1569.

(39) Sen, K.; Schäfer, A.; Rosowski, F.; Sharapa, D. I.; Studt, F. Quantum Chemical Modeling of the Full Catalytic Cycle for Selective Oxidation of Propane to Propene on the M1 Phase of Mo–Te–Nb–O Mixed-Metal Oxide Catalysts. *J. Phys. Chem. C* **2024**, *128* (34), 14273–14281.

(40) Latimer, A. A.; Kulkarni, A. R.; Aljama, H.; Montoya, J. H.; Yoo, J. S.; Tsai, C.; Abild-Pedersen, F.; Studt, F.; Nørskov, J. K. Understanding Trends in C–H Bond Activation in Heterogeneous Catalysis. *Nat. Mater.* **2017**, *16* (2), 225–229.

(41) Abild-Pedersen, F. Computational Catalyst Screening: Scaling, Bond-Order and Catalysis. *Catal. Today* **2016**, *272*, 6–13.

(42) Greeley, J. Theoretical Heterogeneous Catalysis: Scaling Relationships and Computational Catalyst Design. *Annu. Rev. Chem. Biomol. Eng.* **2016**, *7* (1), 605–635.

(43) Furche, F.; Ahlrichs, R.; Hättig, C.; Klopper, W.; Sierka, M.; Weigend, F. Turbomole. *WIREs Comput. Mol. Sci.* **2014**, *4* (2), 91–100.

(44) Ernzerhof, M.; Scuseria, G. E. Assessment of the Perdew–Burke–Ernzerhof Exchange-Correlation Functional. *J. Chem. Phys.* **1999**, *110* (11), 5029–5036.

(45) Perdew, J. P.; Burke, K.; Ernzerhof, M. Generalized Gradient Approximation Made Simple. *Phys. Rev. Lett.* **1996**, *77* (18), 3865–3868.

(46) Weigend, F.; Ahlrichs, R. Balanced Basis Sets of Split Valence, Triple Zeta Valence and Quadruple Zeta Valence Quality for H to Rn: Design and Assessment of Accuracy. *Phys. Chem. Chem. Phys.* **2005**, *7* (18), 3297.

(47) Zhao, Y.; Truhlar, D. G. The M06 Suite of Density Functionals for Main Group Thermochemistry, Thermochemical Kinetics, Noncovalent Interactions, Excited States, and Transition Elements: Two New Functionals and Systematic Testing of Four M06-Class Functionals and 12 Other Functionals. *Theor. Chem. Acc.* **2008**, *120* (1–3), 215–241.

(48) Dinda, S.; Chiu, C.; Genest, A.; Rösch, N. Evaluation of Density Functionals for Elementary Steps of Selective Oxidation Reactions. *Computational and Theoretical Chemistry* **2017**, *1101*, 36–45.

(49) Goncalves, T. J.; Plessow, P. N.; Studt, F. On the Accuracy of Density Functional Theory in Zeolite Catalysis. *ChemCatChem.* **2019**, *11* (17), 4368–4376.

(50) Goerigk, L.; Grimme, S. A Thorough Benchmark of Density Functional Methods for General Main Group Thermochemistry, Kinetics, and Noncovalent Interactions. *Phys. Chem. Chem. Phys.* **2011**, *13* (14), 6670.

(51) Grimme, S.; Antony, J.; Ehrlich, S.; Krieg, H. A Consistent and Accurate *Ab Initio* Parametrization of Density Functional Dispersion Correction (DFT-D) for the 94 Elements H-Pu. *J. Chem. Phys.* **2010**, *132* (15), 154104.

(52) Busch, M.; Fabrizio, A.; Luber, S.; Hutter, J.; Corminboeuf, C. Exploring the Limitation of Molecular Water Oxidation Catalysts. *J. Phys. Chem. C* **2018**, *122* (23), 12404–12412.

(53) Okazaki, I.; Sato, F.; Yoshihiro, T.; Ueno, T.; Kashiwagi, H. Development of a Restricted Open Shell Kohn–Sham Program and Its Application to a Model Heme Complex. *Journal of Molecular Structure: THEOCHEM* **1998**, *451* (1–2), 109–119.

(54) Kubas, A.; Noak, J.; Trunschke, A.; Schlögl, R.; Neese, F.; Maganas, D. A Combined Experimental and Theoretical Spectroscopic Protocol for Determination of the Structure of Heterogeneous Catalysts: Developing the Information Content of the Resonance Raman Spectra of $M1MoVO_x$. *Chem. Sci.* **2017**, *8* (9), 6338–6353.

(55) Tuma, C.; Sauer, J. Treating Dispersion Effects in Extended Systems by Hybrid MP2:DFT Calculations—Protonation of Isobutene in Zeolite Ferrierite. *Phys. Chem. Chem. Phys.* **2006**, *8* (34), 3955–3965.

(56) Svelle, S.; Tuma, C.; Rozanska, X.; Kerber, T.; Sauer, J. Quantum Chemical Modeling of Zeolite-Catalyzed Methylation Reactions: Toward Chemical Accuracy for Barriers. *J. Am. Chem. Soc.* **2009**, *131* (2), 816–825.

(57) Hansen, N.; Kerber, T.; Sauer, J.; Bell, A. T.; Keil, F. J. Quantum Chemical Modeling of Benzene Ethylation over H-ZSM-5 Approaching Chemical Accuracy: A Hybrid MP2:DFT Study. *J. Am. Chem. Soc.* **2010**, *132* (33), 11525–11538.

(58) Korth, M.; Grimme, S. "Mindless" DFT Benchmarking. *J. Chem. Theory Comput.* **2009**, *5* (4), 993–1003.

(59) Gonzalez, C.; Schlegel, H. B. Reaction Path Following in Mass-Weighted Internal Coordinates. *J. Phys. Chem.* **1990**, *94* (14), 5523–5527.

(60) Staroverov, V. N.; Scuseria, G. E.; Tao, J.; Perdew, J. P. Comparative Assessment of a New Nonempirical Density Functional: Molecules and Hydrogen-Bonded Complexes. *J. Chem. Phys.* **2003**, *119* (23), 12129–12137.

(61) Schäfer, A.; Huber, C.; Ahlrichs, R. Fully Optimized Contracted Gaussian Basis Sets of Triple Zeta Valence Quality for Atoms Li to Kr. *J. Chem. Phys.* **1994**, *100* (8), 5829–5835.

(62) Deshlahra, P.; Iglesia, E. Toward More Complete Descriptors of Reactivity in Catalysis by Solid Acids. *ACS Catal.* **2016**, *6* (8), 5386–5392.

(63) Xu, J.; Cao, X.-M.; Hu, P. Improved Prediction for the Methane Activation Mechanism on Rutile Metal Oxides by a Machine Learning Model with Geometrical Descriptors. *J. Phys. Chem. C* **2019**, *123* (47), 28802–28810.

(64) Plessow, P. N.; Studt, F. How Accurately Do Approximate Density Functionals Predict Trends in Acidic Zeolite Catalysis? *J. Phys. Chem. Lett.* **2020**, *11* (11), 4305–4310.

(65) Amsler, J.; Sarma, B. B.; Agostini, G.; Prieto, G.; Plessow, P. N.; Studt, F. Prospects of Heterogeneous Hydroformylation with Supported Single Atom Catalysts. *J. Am. Chem. Soc.* **2020**, *142* (11), 5087–5096.

(66) Liu, Y.; Annamalai, L.; Deshlahra, P. Effects of Lattice O Atom Coordination and Pore Confinement on Selectivity Limitations for

Ethane Oxidative Dehydrogenation Catalyzed by Vanadium-Oxo Species. *J. Phys. Chem. C* **2019**, *123* (46), 28168−28191.

(67) Annamalai, L.; Ezenwa, S.; Dang, Y.; Tan, H.; Suib, S. L.; Deshlahra, P. Comparison of Structural and Catalytic Properties of Monometallic Mo and V Oxides and M1 Phase Mixed Oxides for Oxidative Dehydrogenation. *Catal. Today* **2021**, *368*, 28−45.

(68) Naumann d'Alnoncourt, R.; Kolen'ko, V. Y.; Schlogl, R.; Trunschke, A. A New Way of Probing Reaction Networks: Analyzing Multidimensional Parameter Space. *Comb. Chem. High Throughput Screening* **2012**, *15* (2), 161−169.

(69) Gaffney, A. M.; An, Q.; Goddard, W. A.; Diao, W.; Glazoff, M. V. Toward Concurrent Engineering of the M1-Based Catalytic Systems for Oxidative Dehydrogenation (ODH) of Alkanes. *Top Catal* **2020**, *63* (19−20), 1667−1681.

(70) Goddard, W. A. Quantum Mechanics Based Mechanisms for Selective Activation of Hydrocarbons by Mixed Metal Oxide Heterogeneous Catalysts − A Tribute to Robert Grasselli. *Catal. Today* **2021**, *363*, 3−9.

(71) Zhu, Y.; Jensen, E.; Sushko, P. V.; Kovarik, L.; Sanchez-Sanchez, M.; Lercher, J. A.; Melzer, D.; Ophus, C.; Browning, N. D. The Merits of In Situ Environmental STEM for the Study of Complex Oxide Catalysts at Work. *Microsc Microanal* **2018**, *24* (S1), 238−239.

(72) Melzer, D.; Mestl, G.; Wanninger, K.; Jentys, A.; Sanchez-Sanchez, M.; Lercher, J. A. On the Promoting Effects of Te and Nb in the Activity and Selectivity of M1MoV-Oxides for Ethane Oxidative Dehydrogenation. *Top Catal* **2020**, *63* (19−20), 1754−1764.

(73) Zhu, Y.; Sushko, P. V.; Melzer, D.; Jensen, E.; Kovarik, L.; Ophus, C.; Sanchez-Sanchez, M.; Lercher, J. A.; Browning, N. D. Formation of Oxygen Radical Sites on MoVNbTeOx by Cooperative Electron Redistribution. *J. Am. Chem. Soc.* **2017**, *139* (36), 12342−12345.

(74) Melzer, D.; Mestl, G.; Wanninger, K.; Zhu, Y.; Browning, N. D.; Sanchez-Sanchez, M.; Lercher, J. A. Design and Synthesis of Highly Active MoVTeNb-Oxides for Ethane Oxidative Dehydrogenation. *Nat. Commun.* **2019**, *10* (1), 4012.

(75) Melzer, D.; Xu, P.; Hartmann, D.; Zhu, Y.; Browning, N. D.; Sanchez-Sanchez, M.; Lercher, J. A. Atomic-Scale Determination of Active Facets on the MoVTeNb Oxide M1 Phase and Their Intrinsic Catalytic Activity for Ethane Oxidative Dehydrogenation. *Angew. Chem., Int. Ed.* **2016**, *55* (31), 8873−8877.

(76) Li, W.; Fjermestad, T.; Genest, A.; Rösch, N. How the Distribution of Reduced Vanadium Centers Affects Structure and Stability of the MoVO$_x$ Material. *Catal. Sci. Technol.* **2018**, *8* (10), 2654−2660.

(77) Arce-Ramos, J. M.; Rugg, G.; Genest, A.; Rösch, N. Probing the Positions of TeO Moieties in the Channels of the MoVNbTeO M1 Catalyst: A Density Functional Theory Model Study. *Catal. Lett.* **2021**, *151* (10), 2884−2893.

(78) Fjermestad, T.; Li, W.-Q.; Genest, A.; Rösch, N. Configurations of V4+ Centers in the MoVO Catalyst Material. A Systematic Stability Analysis of DFT Results. *SN Appl. Sci.* **2020**, *2* (11), 1909.

(79) Fjermestad, T.; Li, W.; Rugg, G.; Ishida, S.; Okuno, M.; Sagi, K.; Genest, A.; Rösch, N. Acrolein Oxidation to Acrylic Acid over the MoVOx Material. Insights from DFT Modeling. *Applied Catalysis A: General* **2018**, *565*, 68−75.

(80) Pyrz, W. D.; Blom, D. A.; Vogt, T.; Buttrey, D. J. Direct Imaging of the MoVTeNbO M1 Phase Using An Aberration-Corrected High-Resolution Scanning Transmission Electron Microscope. *Angew. Chem., Int. Ed.* **2008**, *47* (15), 2788−2791.

(81) Blom, D. A.; Vogt, T. Multi-Slice Frozen Phonon Simulations of High-Angle Annular Dark Field Scanning Transmission Electron Microscopy Images of the Structurally and Compositionally Complex Mo−V−Nb−Te Oxide Catalyst. *Adv. Struct Chem. Imag* **2018**, *4* (1), 9.

(82) Aouine, M.; Epicier, T.; Millet, J.-M. M. In Situ Environmental STEM Study of the MoVTe Oxide M1 Phase Catalysts for Ethane Oxidative Dehydrogenation. *ACS Catal.* **2016**, *6* (7), 4775−4781.

(83) Kardash, T. Y.; Lazareva, E. V.; Svintsitskiy, D. A.; Ishchenko, A. V.; Bondareva, V. M.; Neder, R. B. The Evolution of the M1 Local Structure during Preparation of VMoNbTeO Catalysts for Ethane Oxidative Dehydrogenation to Ethylene. *RSC Adv.* **2018**, *8* (63), 35903−35916.

(84) Pyrz, W. D.; Blom, D. A.; Shiju, N. R.; Guliants, V. V.; Vogt, T.; Buttrey, D. J. Using Aberration-Corrected STEM Imaging to Explore Chemical and Structural Variations in the M1 Phase of the MoVNbTeO Oxidation Catalyst. *J. Phys. Chem. C* **2008**, *112* (27), 10043−10049.